SOCIETY FOR APPLIED SPECTROSCOPY

Applied Spectroscopy
1–13

DOI: 10.1177/00037028251399225
journals.sagepub.com/home/asp
Sage

Extension of Complex Refractive Index Measurements to the Near-Infrared for Liquids: Methodology and Uncertainty Analysis

Oliva M. Primera-Pedrozo[1], Russell G. Tonkyn, Tracy J. Baker[1], Schuyler P. Lockwood[1], Ashley M. Bradley[1], Timothy J. Johnson[1], and Tanya L. Myers[1]

Abstract

Optical identification of liquid droplets, aerosols, or thin films is critical for many applications. While reference spectra are sometimes available for such measurements, they are not always applicable to the observed spectrum or the given sample morphology. Reference spectra for many forms can be modeled, however, if the *n*/*k* vectors (real and imaginary refractive indices) are available. In previous work we have reported protocols to determine the *n*/*k* vectors for dozens of liquids, primarily in the mid-infrared (MIR) spectral range from 7500 to 400 cm^{-1}. In this work we extend the spectral range into the near-infrared (NIR) region, demonstrating a method to measure and merge the data sets to create composite *n*/*k* data ranging from 10 000 to 400 cm^{-1} (1.0 to 25 μm) with absorbance fidelity spanning over four orders of magnitude, and vastly improved signal-to-noise in the NIR. The precision of the composite data is evaluated for three different liquids, focusing primarily on the steps for converting the raw absorbance spectra to *k* values. The variability in both MIR and NIR data as well as in the final *n*/*k* vectors is also investigated for several liquids. For typical liquids, the overall variability (reported as 2σ) in the final *n* and *k*-vectors is determined to be ~0.4% and 3%, respectively. Finally, the derived *n*/*k* data are used to calculate absorbance spectra for aerosol droplets, showing marginal variability due to the typical measurement errors in the final *n*/*k* vectors.

Keywords

Optical constants, complex refractive index, near-infrared, NIR, liquids, database

Date received: 23 August 2025; accepted: 29 October 2025

Introduction

Infrared (IR) spectroscopy is a valuable analytical tool for detection and identification of solids, liquids, and gases.[1–17] In real-world scenarios, liquids can exist as bulk, as droplets or as films on different substrates. The droplet size and shape as well as the film thickness and the substrate properties can significantly alter the IR reflectance, emission and transmission[18–23] spectra, making identification problematic if, e.g., only the spectrum of the bulk material is available in a reference library. Use of the bulk material's complex refractive index ($\tilde{n} = n + ik$), however, allows for accurate spectral modeling to account for such morphological effects.[24,25] Consequently, the development of spectral libraries that include both the real (*n*) and imaginary (*k*) components of the complex refractive index as a function of IR wavenumber ν (or wavelength λ) provides a robust solution to account for these environmental and morphological variations.[13]

In particular, the mid-infrared (MIR) region, spanning from 4000 to 400 cm^{-1}, is exceptionally useful for (trace) detection, as it contains the strong fundamental vibrational absorption bands (largest *k* values) of most chemical species. MIR spectroscopy is thus a powerful tool for analyzing complex mixtures or identifying materials, even at low concentrations.[26–28] On the other hand, the near-infrared (NIR) region (10 000–4000 cm^{-1}) features weaker overtone and combination bands[29–35] that are still useful for the analysis of higher concentration samples where the fundamental MIR absorption bands may be saturated. Moreover, combining

[1]Pacific Northwest National Laboratory, 902 Battelle Boulevard, Richland, Washington, USA

Corresponding Author:
Tanya L. Myers, Pacific Northwest National Laboratory, 902 Battelle Boulevard, Richland, Washington 99352, USA.
Email: Tanya.Myers@pnnl.gov

spectral data from both the MIR and NIR regions enhances the accuracy and confidence of material detection and identification, as it provides complementary spectral information.

In earlier work,[21] protocols were established for measuring the complex refractive indices for 57 liquids spanning the MIR from 7800 to 400 cm^{-1}; these *n*/*k* data are available for download.[36] This work expands that effort to (i) include a larger number of liquids (Table S1, Supplemental Material), (ii) extend the spectral range into the NIR to 10 000 cm^{-1}, and (iii) estimate the uncertainties in the derived *n*/*k* values. Expanding the spectral range,[37] however, required the use of a second spectrometer system optimized for shorter wavelengths. A single multi-range instrument could of course be used with requisite exchange of optical components, but for the high sample throughput of this study, a second system proved to be more efficient. The second Fourier transform infrared (FT-IR) system utilized an alternate light source and beamsplitter optimized for NIR measurements. Developing protocols for the NIR spectral range greatly improved both the signal-to-noise ratio (SNR) and accuracy for the $n(\nu)$ and $k(\nu)$ values above approximately 4000 cm^{-1}.

In addition, the calculation of $n(\nu)$ and $k(\nu)$ requires several steps, each introducing some uncertainty. These steps include measurement of the refractive index, calculation of effective path lengths, merging of *k* vectors, and performing baseline corrections. Some of the steps require subjective judgment from the analyst; to quantify some of these effects, the variability was examined by having three individuals independently process spectra from three liquid samples: furfural, 2-methylcyclohexanol, and tetraethylene glycol. The resulting variabilities and error estimates for $n(\nu)$ and $k(\nu)$ are reported for these test cases along with the impact on the simulated absorbance spectra for aerosol droplets of 2-methylcyclohexanol.

Experimental

Materials and Methods

The measurement protocols are largely based on earlier works by Bertie et al.[38–43] as improved by Myers et al.[23] for the 7800–400 cm^{-1} region.[21] A brief review is provided here, highlighting the changes required to expand the spectral range to 10 000 cm^{-1}. Most modern FT-IR manufacturers offer NIR capabilities, typically using beamsplitters with either Ge or Si refractive layers coated atop quartz or CaF_2 substrates. The present work used largely Ge/CaF_2 or "extended range" Ge/KBr beamsplitters, and a quartz tungsten bulb as the source. For signal linearity, all instruments used a deuterated l-alanine doped triglycine sulfate detector. Most of the NIR measurements were recorded with either a Bruker Vertex 70 or Tensor 37 instrument. Daily calibrations for both the abscissa (wavenumber) and ordinate (intensity) responses are performed, as has been previously described.[44,45]

The liquid absorbance spectra are measured using commercially available transmission cells of varied path length to span the dynamic range of both strong and weak absorption features. For most measurements potassium bromide (KBr) or potassium chloride (KCl) cells are employed. For aqueous species, either quartz, CaF_2 or ZnSe may be used to non-reactively contain the liquid. For example, tetraethylene glycol showed spectral shifts for the O–H bands with KBr cells due to the hydroxyl groups interacting with the cells (see Figure S1, Supplemental Material).

Due to the weaker NIR absorptions, five or six cells with longer path lengths are used, typically path lengths on the order of 100, 200, 500, 1000, 2000, and 4000 μm. In the MIR, six to seven cells are used with paths typically around 2, 5, 10, 20, 50, 100, 200, and 500 μm.[46] The same ~100, 200, and 500 μm cells containing the same liquid fill are measured with both the MIR and NIR spectrometers. For the shortest path cells (< 20 μm), flat KBr windows are pressed together without a gasket over a thin film of sample. The path length of each cell is determined by combining the fringe pattern measured with an empty cell with iterative fitting to the Beer–Lambert law.[21,44] For certain absorption bands multiple iterations are sometimes required to minimize the difference between the fringe-calculated path lengths vs. those derived using the Beer–Lambert law. Multiple measurements are recorded at each path to ensure the signal is invariant with time. The high-purity liquids are injected via syringe into the cells, and the absorbance spectrum is recorded using a spectral resolution of 2 cm^{-1} with a digital point every 0.4821 cm^{-1}. Additional parameters are detailed in the Supplemental Material (Table S2) for both the NIR and MIR instruments. The liquid sample cell is rotated at 7° relative to beam normal to minimize back-reflection artifacts.[47]

Refractometry Measurements

Kramers–Kronig relations are applied to relate the real and imaginary parts of the complex refractive index and yield a consistent set of $n(\nu)$ and $k(\nu)$ values. In particular, the $n(\nu)$ vector is derived from the $k(\nu)$ vector via the Kramers–Kronig transform (KKT).[21,41,44,48] A key component in the analysis is the scalar refractive index, $n(\nu_{max})$, that is used as a boundary condition in the KKT where ν_{max} is the maximal wavenumber recorded in the FT-IR spectrum.[41] The liquid scalar refractive index, $n(\lambda)$, is measured at multiple wavelengths using a temperature-controlled Abbe refractometer (Atago) with notch filters centered at 0.480, 0.486, 0.546, 0.589, 0.644, 0.656, and 1.55 μm. To observe the near-IR wavelength, a viewer is used at 1.55 μm. The data are fit to a modified Sellmeier equation,[21,49] so as to calculate $n(\nu_{max})$ for the MIR and NIR experimental data at 7800 cm^{-1} (1.28 μm), and 10 000 cm^{-1} (1.0 μm), respectively.

Theoretical–Aerosol Spectral Predictions

A Mie theory-based Matlab package developed by Schäfer[50,51] was used to compute synthetic absorption data for an aerosol

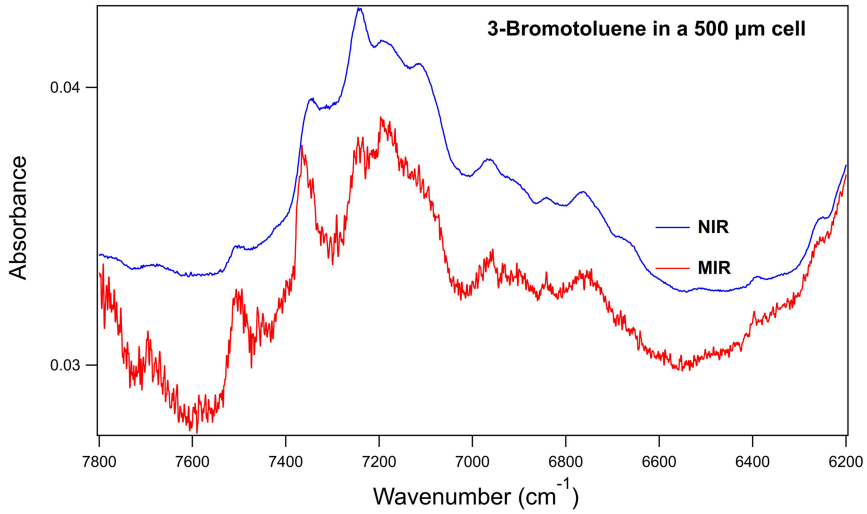

Figure 1. Absorbance spectra of 3-bromotoluene measured with a 500 µm cell and instruments optimized for either the NIR (top) or MIR (bottom) spectral range. Only the NIR data are used in this spectral region to provide good SNR. Spectra are vertically offset for clarity.

of 2-methylcyclohexanol. Using only the Mie equations along with inputs of the complex refractive index of the desired material, the frequency of light, and the droplet diameter, the package computes the extinction cross-section (σ_{ext}) for a spherical droplet. For purposes of generating spectral data for an ensemble of droplets, this computation of σ_{ext} at a single frequency and droplet diameter is repeated over the entire frequency and diameter ranges of interest and scaled according to the number densities in a droplet size distribution to obtain the ensemble weighted average extinction cross-section ($\sigma_{ext,avg}$) as a function of frequency. The cross-section vector is multiplied by the total number density of the droplet ensemble and the path length through the aerosol to obtain the absorption spectrum.[45]

Results and Discussion

Expanded Spectral Domain: 10 000–4000 cm^{-1}

The salient result of this paper is the extension of the spectral range of quantitative *n* and *k* optical vector data into the near-IR, namely from 10 000 to 4000 cm^{-1} (1.0–2.5 µm). These new protocols augment earlier work[21] that only included measurements in the MIR from 7800 cm^{-1} to 400 cm^{-1} by extending the spectral range into the NIR and significantly improving the accuracy and SNR of the data above 4000 cm^{-1}. The NIR data are then merged with the MIR data to form a composite spectrum, providing good SNR across the entire range. An example of the improved SNR is seen in Figure 1 for 3-bromotoluene in the region between 7800 and 6200 cm^{-1}. Especially at high wavenumber the increase in the SNR is impressive and can exceed tenfold, along with better spectral baseline stability.

The availability of $n(\nu)$ and $k(\nu)$ data, along with their quantified uncertainties, is required to model the spectral variability of aerosols[45,52,53] and thin films.[24,25,48] As part of a larger project, and as summarized in the Table S1 (Supplemental Material), measurements of *n*/*k* have thus been conducted for over 100 liquids in the spectral range from 10 000 to 400 cm^{-1} at 2.0 cm^{-1} spectral resolution. Expanding the spectral range into the NIR has provided significant advantages, including over a tenfold improvement in the SNR above 6500 cm^{-1}, and the ability to measure weak spectral features above 7800 cm^{-1}.

Estimating Uncertainty

Reducing the raw absorption spectra into the *n* and *k* vectors is a stepwise and relatively straightforward process but does require some subjective judgment by the analyst during, e.g., the path length estimates, the baseline corrections, and the spectral merging steps. The overall uncertainty in the derived *n* and *k* vectors is therefore a combination of measurement uncertainty and processing variability. To better understand the variability introduced by these processes, a study was conducted whereby three different analysts independently processed the data for each liquid sample using furfural, 2-methylcyclohexanol, and tetraethylene glycol. A fourth scenario was introduced where one analyst reprocessed a subset of the data several months after the initial analysis. We combine the results of the variability due to the analysis with estimated measurement uncertainty to derive the overall uncertainty in *n* and *k*.

Figure 2 illustrates the normalized absorption spectra for these three liquids, each offset for clarity. The three liquids were specifically selected to cover a range of spectral complexities as well as data-processing challenges due to, e.g., peak intensities, widths, and spacing. Furfural was selected

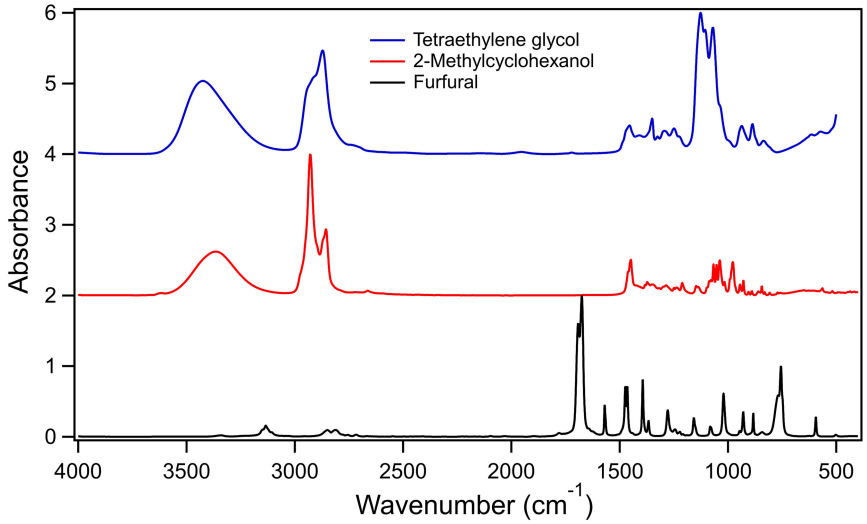

Figure 2. Normalized absorbance spectra of the three test cases chosen for variability tests: furfural (bottom), 2-methylcyclohexanol (center) and tetraethylene glycol (top). The spectra are calculated from the final *k* vectors, normalized 0.0 to 2.0, and vertically offset for clarity.

as the "ideal" test case due to its distinct, well-isolated spectral peaks that simplify processing and minimize ambiguity. 2-Methylcyclohexanol was selected to represent the typical liquid where the absorption spectra exhibit broad bands with relatively strong signal intensities except in the low wavenumber regions where the features are less distinct, introducing moderate data-processing challenges. Finally, tetraethylene glycol, due to its complex spectral profile and chemical nature, was the most challenging to process as this liquid required the use of three different cell materials (ZnSe, CaF_2, KCl) to span its full spectral range. Furthermore, the spectra contain few distinct bands that can be reliably used to establish ratios between the long and short cells; these ratios are used to yield better estimates of the path lengths as discussed in the Variability in the Path-Length Determination, Δd section below.

The $k(\nu)$ vector is derived from the composite absorption spectrum. The $n(\nu)$ vector is derived from the $k(\nu)$ vector via the KKT. The overall uncertainties in the *n*/*k* data for these species are thus estimated in the following sections. Sources of uncertainties that we considered include sample purity, measurement variabilities, and certain data processing steps. By systematically evaluating the impact of each processing step, comprehensive uncertainty estimates for *n* and *k* are derived.

Uncertainty in $n(\nu_{max})$

To perform the KKT, a scalar *n* value is needed for $n(\infty)$, taken as the maximal wavenumber in the FT-IR measurement,[41,54] $n(\nu_{max})$, which is typically 10 000 cm^{-1} for the liquids used in this study. The scalar refractive index, $n(\nu_{max})$, plays a dual role in the overall calculation: It is first required in the determination of each individual *k* vector, and then it is used again to compute the final $n(\nu)$ from the final composite $k(\nu)$ vector via the KKT. This value is obtained experimentally using a temperature-regulated Abbe refractometer to measure the real refractive index, $n(\lambda)$, at seven wavelengths that bracket the target value.[21,44] These scalar *n*-value measurements are subsequently fit to a Sellmeier-type curve[21,49] as seen in Figure 3 to interpolate $n(\nu_{max})$. Although the refractometer has readouts to four decimal places, the visual determination of the light/dark boundary where *n* is measured on a refractometer at a given wavelength can be subjective, particularly for the shorter and longer wavelengths that have lower contrast. The averages and standard deviations for the refractometer readings for tetraethylene glycol as measured by four independent operators are presented in Table S3 (Supplemental Material). The variability in the scalar *n* measurements between researchers is typically $\Delta n \leq 0.001$ for most of the visible wavelengths but is often greater for the 1.55 μm measurement. This NIR wavelength is more challenging to observe since it requires an IR viewer, and the contrast is much weaker.

The uncertainty in the 1.55 μm measurement (±0.002), leads to variability for the interpolated value at 1.0 μm (10 000 cm^{-1}) of ±0.0009. Based on this analysis, we conservatively estimate the uncertainty in $n(\nu_{max})$ to be ±0.002. As demonstrated in Supplemental Material (Figure S2), this uncertainty of $n(\nu_{max})$ produces only small vertical offsets to the final *n* vector and yields marginal changes to the derived *k* vector. The maximum change in *k* for the case shown is 0.2%, with even smaller changes occurring in regions with measurable absorption.

Variability in the Path-Length Determination, Δd

The uncertainty in a cell's path length *d* is a major contributor to the overall uncertainty in the *k* vector calculation, as seen in the relationship of Eq. 1:

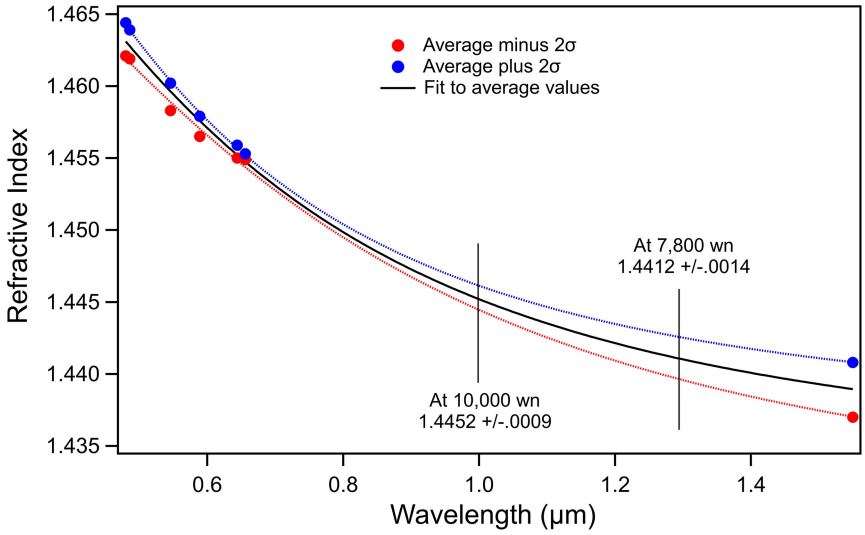

Figure 3. Plot of the measured average refractive index values (solid line) for tetraethylene glycol by four independent researchers using an Abbe refractometer. The dotted lines represent the variability (±2σ) in the measured values. The intersections with the two vertical lines represent the interpolated values at 10 000 cm^{-1} and 7800 cm^{-1}.

$$k = \frac{2.303A(\nu)}{4\pi\nu d} \quad (1)$$

where d is the path length, A is the decadic absorbance, and ν is the wavenumber.[23,41] This equation emphasizes the critical role of accurate path length determination in calculating the k vectors.

In practice, the determination of the path length d is a two-step process.[21] First, the empty cell spectrum is recorded, resulting in a series of étalon fringe spacings. The cell path lengths are calculated by measuring the peak positions of each fringe maximum and calculating an average path length from the spacings. This method is most effective for cells with an approximately 50 to 500 μm gap. Estimating fringe patterns becomes challenging, however, for path lengths shorter than 50 μm due to (i) the increased fringe spacing, (ii) sloping baselines, and (iii) the presence of atmospheric interferents, all of which can obfuscate the fringe features. Moreover, short path length cells often distend when filled, as the pressure required to introduce the liquid can push the windows apart. For path lengths exceeding 500 μm, the fringes become so closely spaced that they are challenging to resolve at 2 cm^{-1} resolution. Especially for the shorter cells, the measured spectra are used along with the Beer–Lambert law to determine the relative path lengths of the filled cells. The absolute path lengths are then fixed by finding the best fit of the relative path lengths to the longer empty cell measurements.

Table I presents the results of three independent empty cell determinations derived from the same set of raw data, processed separately for both the NIR and MIR regions. The table compares the analyses conducted by three different researchers, labeled as R1, R2, R3, and R4 reflects the results of one researcher reprocessing the same dataset several months later, assessing the consistency and repeatability of the method. The agreement between operators typically remains within 1% (2σ). Independent measurements are made with both the MIR and NIR instruments for the overlapping path lengths. The agreement is usually within 0.1%, demonstrating a very high level of consistency between the separate instruments.

Once the empty cell measurements are made, multiple absorbance spectra are collected for each filled cell; a subset of these is chosen for averaging. Spectra exhibiting excessive CO_2/H_2O interference peaks are excluded along with any data suggesting signal drift. Each analyst determines which spectra to include in the averaging process. Variations in the resulting band integrals contribute to variability in the

Table I. Variability in path lengths calculated from empty cell fringe spacing from three independent researchers (R1–R3) for 2-methylcyclohexanol. R4 represents one of the analysts reprocessing the same data months later.

Empty cell path lengths (μm)						
R1	R2	R3	R4	Avg.	Standard deviation (2σ)	% Standard deviation (2σ)
MIR						
106.7	107.1	106.5	105.7	106.5	1.02	0.96
180.2	180.1	180.3	180.8	180.3	0.54	0.30
467.4	467.5	467.5	466.7	467.3	0.68	0.14
NIR						
106.7	106.3	106.3	106.4	106.4	0.33	0.31
180.1	180.1	180.0	180.4	180.2	0.30	0.17
468.1	467.4	467.7	467.1	467.6	0.74	0.16

Table II. Variability in path lengths as calculated from Beer–Lambert law plots for 2-methylcyclohexanol as determined by three different analysts. R4 represents one of the researchers reprocessing the same data months later. The shaded cells correspond to identical cells being used for both the MIR and NIR measurements. The MIR and NIR were analyzed independently.

Path length results (μm)						
R1	R2	R3	R4	Avg.	Standard deviation (2σ)	% Standard deviation (2σ)
MIR						
4.13	4.05	4.04	4.01	4.06	0.09	2.3
5.85	5.80	5.80	5.80	5.81	0.04	0.7
24.1	24.0	23.9	24.0	24.0	0.1	0.5
24.2	24.0	24.1	24.1	24.1	0.1	0.5
30.0	29.8	30.1	29.9	30.0	0.2	0.6
47.3	47.4	47.7	47.6	47.5	0.3	0.6
106.9	107.0	107.1	107.1	107.0	0.2	0.2
180.2	180.2	180.2	179.9	180.1	0.3	0.1
466.9	467.2	466.4	465.5	466.5	1.3	0.3
NIR						
106.5	106.8	107.1	106.9	106.8	0.4	0.4
180.0	181.9	180.3	180.4	180.7	1.5	0.8
468.3	467.6	466.6	466.5	467.3	1.5	0.3
919.1	925.4	920.7	920	921.3	4.9	0.5
2059	2062	2070	2066	2064	8.3	0.4

final *k* vector calculation through the analysis. The Supplemental Material (Table S4) presents results for 2-methylcyclohexanol showing comparisons among the average spectra for three different path lengths (~4, 47, 467 μm) determined by four analysts. The differences are small, with the 2σ standard deviation for the integrated band area being ≤ 0.5%. Similar results were obtained for furfural and tetraethylene glycol, included in Tables S5 and S6, respectively (Supplemental Material).

As discussed, first estimates of cell path length are calculated from empty cell fringing patterns. To better refine the cell path length value, the Beer–Lambert law is applied:

$$A(\nu) = (\varepsilon(\nu) * c) * d \quad (2)$$

where A(ν) represents the decadic absorbance at wavenumber ν, ε(ν) is the extinction coefficient, *c* is the concentration, and *d* is the path length. While the product of ε(ν) * *c* is unknown, it remains constant across all measurements for a given pure material. Therefore, A(ν) is proportional to the path length *d*, and the ratio of two absorbances yields the ratio of path lengths directly. The absolute values of *d* are determined by finding the best fit of the ratios to the empty cell results for cells with longer path lengths, which are presumed to be the most accurate.

Due to the significant variation in absorption band strength, weaker bands, especially in the near–infrared, are analyzed using data from the long path length cells, while stronger bands are analyzed using primarily short-cell data. It is necessary to employ bands of intermediate absorption strength to "bridge" the relative path length calculation (using Beer–Lambert law) between long and short cells. Each analyst determines which regions to integrate and selects the appropriate path cells for each region. The results shown in Table II demonstrate that the analysts' agreement was quite good, with a standard deviation (2σ) of less than 1% for all but the shortest path lengths. The data also show good agreement between the MIR and NIR domains. Detailed results for furfural and tetraethylene glycol are described in Tables S7 and S8, respectively (Supplemental Material). Given the results shown, we estimate an overall uncertainty in the cell path length to be $\Delta d = \pm 1\%$ in most cases. Extremely strong bands, loosely defined as those that saturate for path lengths > 10 μm, will require the use of shorter cells and will have greater uncertainty. Due to the factor of *v* in Eq. 1, this occurs when $k^*\nu \sim 300$ or greater. For these spectral regions we estimate a path length uncertainty of $\Delta d = \pm 2\%$.

Variability in the k Vector Calculation, Δk

The calculation of $k(\nu)$ for each cell is carried out by the program RNJ46A developed by Bertie et al.[41,43] and Sharpe et al.[46] The program requires three key inputs including (i) the path length *d* for each cell, (ii) the "infinite" wavenumber scalar refractive index $n(\infty)$, and (iii) the cell window material. Using an iterative method, the program generates a consistent set of $k(\nu)$ and $n(\nu)$ values that accurately reproduce the experimental spectrum for that cell, while correcting for the reflections from the cell windows. In principle, each $k(\nu)$ should be identical for a given wavelength regardless of path length. Practical deviations occur, however, as

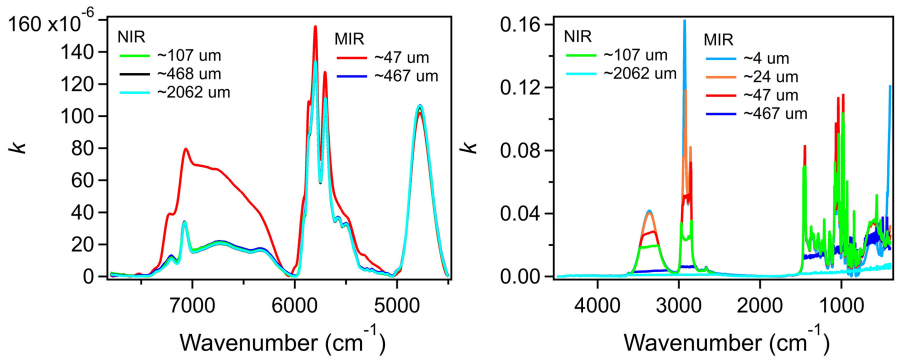

Figure 4. Calculated $k(\nu)$ values for 2-methylcyclohexanol using various path length cells in the MIR. The short path length cells (< 50 μm) do not provide sufficient SNR above 4000 cm^{-1} (left) whereas the long path length cells (> 100 μm) exhibit saturation effects below 4000 cm^{-1} (right).

illustrated in Figure 4. The 47 μm cell, which exhibits almost no signal in the 6000 to 7000 cm^{-1} region, produces an exaggerated artifact from 6100 to 7400 cm^{-1} (red trace, left plot in Figure 4). Conversely, the 2062 μm cell shows erroneous k data as the spectrum is saturated below approximately 3700 cm^{-1} (cyan trace, right plot in Figure 4). The approach to merging such disparate k vectors has been discussed in a previous work.[21,44] Briefly, the $k(\nu)$ values are averaged from regions with good signal-to-noise, excluding spectra that are either saturated or lack measurable signal in that region. This is achieved by (i) using a range of cells with different path lengths, (ii) weighting the individual absorbance values by T^2 (transmission squared), and (iii) assigning zero weight for any decadic absorbance[44] values ≥ 2.5. For the present data, the 47 μm data are excluded at high energy (i.e., frequencies greater than approximately 4000 cm^{-1}) and the 2062 μm data are disregarded at frequencies less than ~3600 cm^{-1}; the data are then merged to yield a single $k(\nu)$ vector covering the entire spectral range. In general, the regions and spectra to choose for the merge are reasonably clear, and different operators tend to make similar choices.

The k vector calculated by the RNJ46A program can have considerable baseline curvature leading to negative k values (a physical impossibility). Moreover, the correction for étalon effects due to the cell windows is not perfect and can produce fringes in baseline regions of the k vector that are not present in the original spectra. To derive more physically plausible results, the baseline is corrected, and fringing is removed via smoothing before a final k vector is derived. Typically, the baseline is adjusted using a linear spline between various points on the spectrum; these points are forced through zero by subtracting the line between them. An offset of $+1 \times 10^{-12}$ is then added to the result to ensure k values are positive. The resulting k vector clearly depends on the number and position of the spline fit points. Figure 5 displays the longwave infrared results for $k(\nu)$ for 2-methylcyclohexanol, as calculated from the MIR cells by four analysts. As can be seen, analyst R4 (lower trace in Figure 5) selected a baseline point near 875 cm^{-1}, whereas the other three analysts did not. Incorporating this point into a spline fit baseline correction "pulled down" the entire spectrum. If the baseline points are carefully chosen to be between features the effect on the overall band strength measured "baseline-to-baseline" may not change significantly. In this example, the integrated band strengths agree to within ~1% (2σ).

The final k vector results for the four different analyses (R1–R4) of 2-methylcyclohexanol are plotted in Figure 6. Similar plots for furfural and tetraethylene glycol are presented Figures S3 and S4, respectively (Supplemental Material)). Despite good agreement in the path length determinations, visual inspection of the final k vectors suggest that baseline correction choices can have a significant influence on the result. In the domain $\geq$ 4500 cm^{-1}, less cluttered baseline regions typically result in excellent agreement among the four analysts, especially at larger wavenumber values. In the region from 5000 to 1500 cm^{-1} the agreement remains good, with some variation seen for tetraethylene glycol and 2-methylcyclohexanol (see lower inset in Figure 6). Below 1600 cm^{-1} the agreement is reasonable, but differences caused by baseline correction become apparent, especially at frequencies $\leq$ 1000 cm^{-1} (Figure 5). The results of measuring multiple band strengths for the typical case, i.e., 2-methylcyclohexanol, found the average agreement between the four analysts to be approximately $\Delta k = 1.5\%$ (2σ) across the entire spectral range. The strongest peak located at 2928 cm^{-1} (right inset in Figure 6) also showed significant variability ($\Delta k = 6.3\%$) that did not result from the baseline correction but rather due to the choice of cells used in the processing. One of the analysts (R3) selected only the shortest cell in this spectral region whereas the other three analysts (R1, R2, and R4) used data from the two shortest cells. This difference suggests some non-linearity for this strong peak, highlighting the importance of using several short cells, including some cells with path lengths around 1–2 μm.

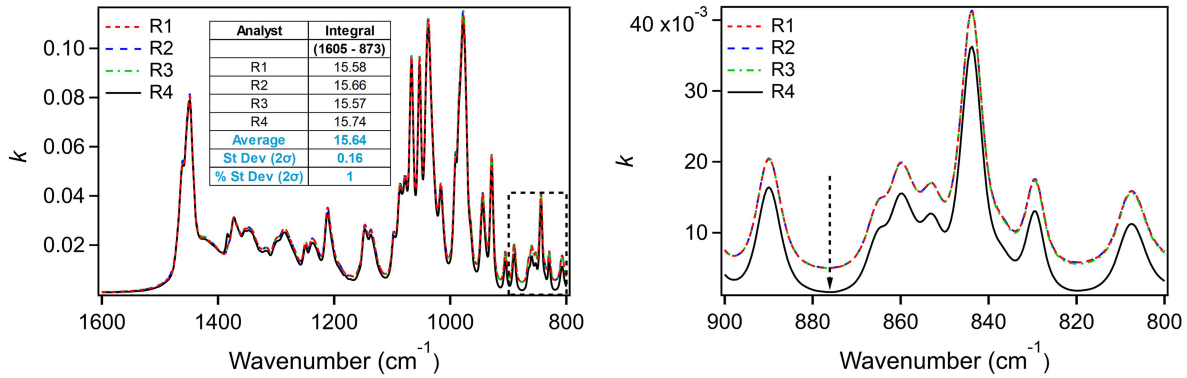

Figure 5. (Left) Comparison of *k* vectors for 2-methylcyclohexanol by different operators. (Right) Expanded region from 900–800 cm^{-1}. Analyst R4 (black trace) chose a baseline point not used by the others near 875 cm^{-1} as indicated by the arrow. The full-spectrum band integrals agree to within 1.0% (2σ).

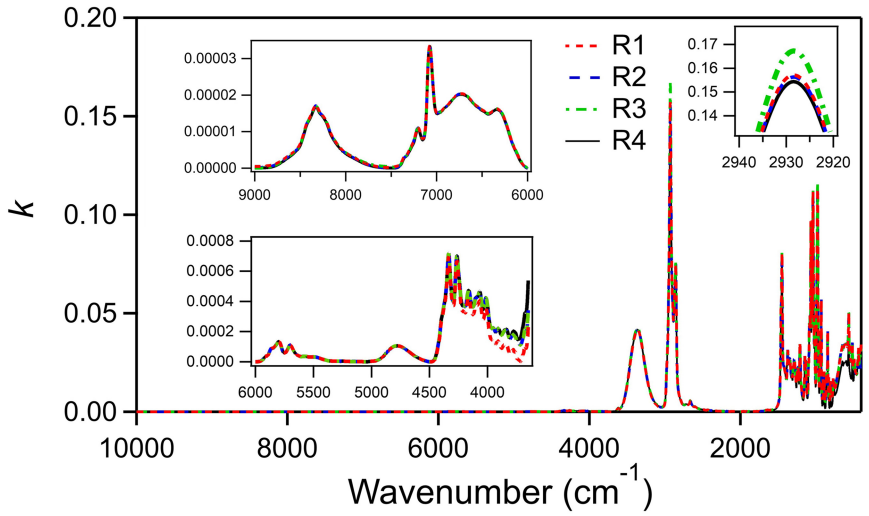

Figure 6. Comparison of *k* calculations by three different operators (R1–R3) for 2-methylcyclohexanol. R4 represents one of the analysts reprocessing the same data months later. As seen in the insets, the overlap is very good in the NIR above 4500 cm^{-1}; the baseline correction can lead to greater variability due to choices made by the processor as indicated in the region around 3700 cm^{-1} (lower left inset) and below 900 cm^{-1} (see Figure 5). The choice of cells can also lead to variability as noted by the difference in peak *k* values near 2928 cm^{-1} (upper right inset).

We note that, as expected, the differences in the *k*-vector are lowest for the ideal case, furfural ($\Delta k = 1.4\%$), and increase to the most challenging case, tetraethylene glycol ($\Delta k = 11.4\%$). For tetraethylene glycol, most of the variation arises from incorporating the analysis with KBr cells, leading to large uncertainties in the OH band regions (see Figures S1 and S3). If the analysis with the KBr cells is excluded, the variability is greatly reduced ($\Delta k = 2.8\%$).

Uncertainty Associated with Merging MIR and NIR k-Vectors

The composite MIR and NIR *k* vectors are merged to generate a final composite *k* vector from 10 000 to 400 cm^{-1} (1–25 μm). Merging the MIR and NIR *k* vectors requires careful selection of the overlap region. Due to lower noise levels, the NIR data are used preferentially at higher wavenumber values. The long path length NIR data typically saturate near 3100 cm^{-1} due to strong C–H stretching bands; only the short path MIR data are used in this domain, i.e., < 3500 cm^{-1}. The final $k(\nu)$ data thus consist of (i) the NIR result above a specified wavenumber, typically >5000 cm^{-1} (ii) an intermediate overlap domain where a weighted average is applied (starting at 0% MIR and gradually increasing to 100% MIR weighting), and finally (iii) the MIR data exclusively used from approximately 3500–400 cm^{-1}. Variability caused by merging different regions is relatively minor and only affects the region around the merge point, which is almost always chosen between absorbance features.

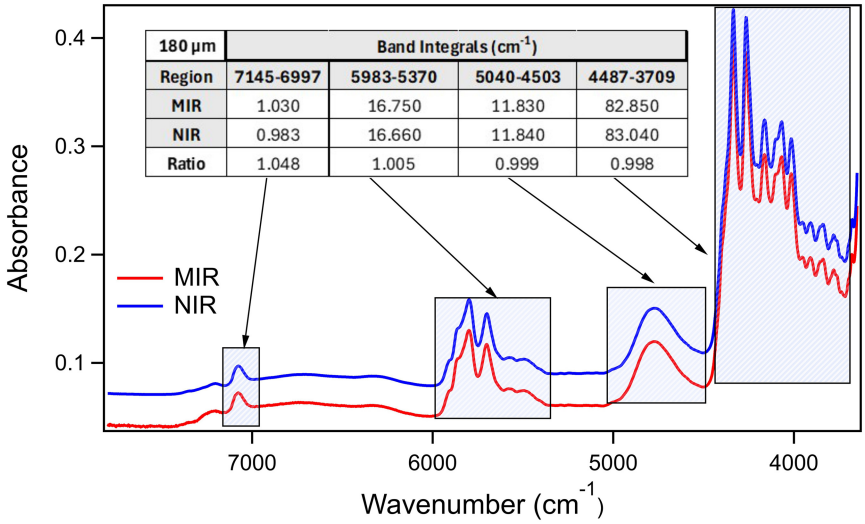

Figure 7. Comparison of long path length spectra taken with MIR and NIR instruments for 2-methylcyclohexanol. Spectra are vertically offset for clarity.

Uncertainty with Sample Purity, Δconc

In most cases, samples are used as obtained from commercial manufacturers and have a stated purity ranging from ≥97% to ≥99%. Without knowing the exact purity level or the nature of the impurities, it is difficult to quantitatively correct for this unknown. In general, the *k* vector values will be underestimated by the impurity percentage. For 2-methylcyclohexanol, for example, the minimum stated purity is ≥98.5%, meaning the amplitudes of the *k* vector may be underestimated by up to 1.5%. If an impurity has strong absorbances, these features may manifest in the final result, but this is not generally observed. In addition, an impurity may impact the refractive index measurements in an unknown manner, especially if the impurity has a significantly different *n*-value. While it is difficult to estimate the magnitude of this error, it is most likely to produce a small vertical offset in the *n* vector. Assuming absorption bands from low level impurities are not present, the *k* vector error is simply proportional to the fraction of impurity (Eq. 2). Based on measurement of hundreds of samples from reputable vendors, we conservatively estimate a typical impurity level of approximately 2%, and thus a *k* vector uncertainty due to chemical impurities of $\Delta conc = 2\%$. This value depends on the specific sample and its purity.

Uncertainty Due to Instrumental Accuracy, Δm

The NIR and MIR measurements (from separate instruments using different sources and beamsplitters) have comparable responses in the region from 6000 to 3200 cm^{-1}. Above 6000 cm^{-1} the MIR results typically become very noisy, and below 3200 cm^{-1} the long path length cells used for the NIR measurements result in saturation and non-linear effects. In the overlap region the results of spectra taken on two instruments using the same filled cell give a sense of the variability one might expect from instrumental differences. Apart from slight baseline offsets, the peak positions and band shapes align nicely as seen in Figure 7, using data from a Bruker Vertex 70 with a NIR W-lamp source and a Bruker Tensor 37 equipped with a glow bar MIR source. The 2-methylcyclohexanol spectra were recorded using the same filled cell on the same day. The results of the measurements for all three overlapping path lengths are given in Supplemental Material (Table S9) for the regions shown in Figure 7. Calculating multiple integrated band areas for all three samples in the 6000–3700 cm^{-1} range resulted in an average agreement of 0.3% with a relative standard deviation (2σ) of $\Delta m = 1.7\%$. For very small absorbances the agreement is poorer, as shown for the absorbance near 7000 cm^{-1}; this discrepancy, however, could also result from the lower SNR for the MIR instrument but does not impact the composite *k*-spectrum since the NIR data are typically only used above 5000 cm^{-1}. The relative variability in the *k* vector band integrals is estimated to be $\Delta m = 1.7\%$.

Estimating Composite Uncertainty, D

To evaluate and quantify the uncertainties inherent in the methods used to derive *n* and *k*, a composite uncertainty is estimated by adding in quadrature[55] the fractional errors discussed above. Table III summarizes an overview of these

Table III. Maximum estimated systematic uncertainties.

Error source	Symbol	Percent value (%)
Determination of $n(\nu_{max})$	Δn_{max}	0.2
k Vector calculation	Δk	1.5
Sample purity	$\Delta conc$	2
Measurement uncertainty	Δm	1.7
Composite uncertainty estimate	D	3

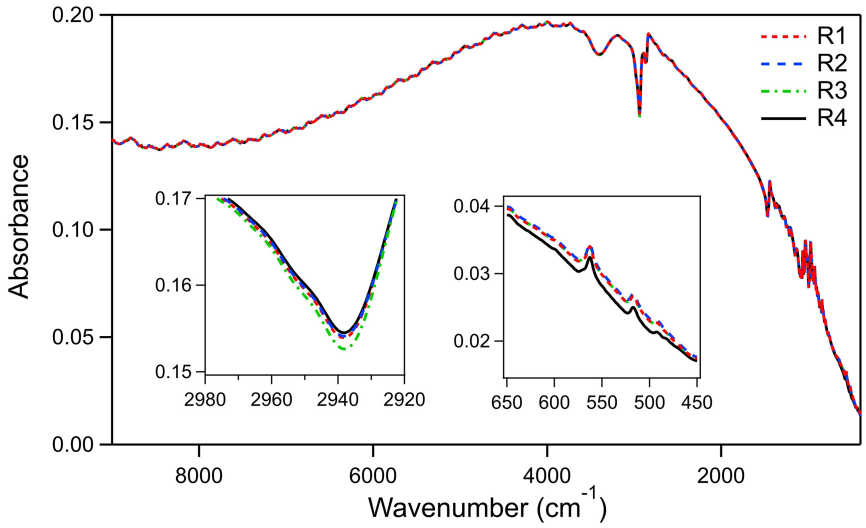

Figure 8. Simulated absorbance of a 10^4 droplets/cm^3 aerosol of 2-methylcyclohexanol through a path length of 10 meters using *n*/*k* vectors derived by three different analysts (R4 represents one of the analysts reprocessing the same data months later). The simulation uses a lognormal size (diameter) distribution with mean $\mu = 4.0$ μm and standard deviation $\sigma = 1.8$ μm.

uncertainty estimates, detailing their sources, and presenting their fractional (percentage) values.

Specifically, Eq. 2 provides a mathematical framework for assimilating the cumulative effects of individual uncertainty sources in deriving the *n* and *k* optical constants. These sources include variations in determination of $n(\nu_{max})$, the *k* vector calculation (which includes the Beer–Lambert law path length (*d*) uncertainty results), the sample purity (*conc*), and measurement uncertainty (*m*).

$$D = [(\Delta n_{max})^2 + (\Delta k)^2 + (\Delta conc)^2 + (\Delta m)^2]^{0.5} \quad (2)$$

Equation 2 yields an overall uncertainty of approximately $D = \pm 3\%$ in the *k* vector for liquid optical vectors analyzed using these protocols. This *k* vector uncertainty does not significantly affect the *n* vector calculation. As shown in Figure S5 (Supplemental Material), changing the *k* vector by 5% changes the calculated *n* vector by less than 0.5% (shows a maximum variability of ±0.3%). The other source of uncertainty is attributed to the determination of $n(\nu_{max})$, which provides an offset to the *n*-spectrum. The typical uncertainty in $n(\nu_{max})$ is estimated to be ±0.002, leading to an uncertainty of ±0.3%. These two uncertainties added in quadrature lead to an overall uncertainty of ±0.4% for the *n* vector.

Variability of the Derived k-Vectors on the Synthetic Data

Knowledge of the $n(\lambda)$ and $k(\lambda)$ optical vectors of a material enables modeling of the many morphological effects, e.g., layer thickness and particle size, which may cause a real-world reflectance, absorption or scattered light spectrum of a material to deviate from that of the bulk (slab transmission) reference spectrum. To assess how variability in the derived *n*/*k* vectors of liquids may impact optical modeling of such deviations from reference data, a series of synthetic spectra were generated from μm-sized spherical liquid droplets in an aerosol cloud. The absorbance values in Figure 8 were generated over a range of 10 000–400 cm^{-1} for a 2-methylcyclohexanol liquid aerosol with a lognormal diameter distribution with a mean of 4.0 μm and a standard deviation of 1.8 μm, a total number density of 10^4 cm^{-3}, and a path length of 10 m.

Distortions to a material's bulk spectral features when aerosolized typically result from the combined contribution of both absorption and scattering phenomena to the transmission spectrum. As seen in Figure 8, these effects, especially scattering, lead to a general increase in absorbance with increasing wavenumber, but also to the emergence of downward-going peaks. Small frequency shifts in the band positions relative to the bulk transmission can also be observed, which is why being able to model the absorbance/transmittance spectra is important to increase detection confidence for stand-off detection of aerosols.[45] These modeled spectra exhibit good agreement between different operator *n*/*k* datasets, demonstrating the typical variability for *n*/*k* data has minimal impact. The largest relative standard deviation for any of the absorbance values (at approximately 2928 cm^{-1} and 575 cm^{-1}, Figure 8) is 6.3%. Virtually no frequency shifts are observed due to variation in the liquid *n*/*k* data. This observation contrasts with other instances (e.g., solids), where relatively larger experimental uncertainties[13] in *n*/*k* led to far greater frequency shifts in generated synthetic data for aerosols of solid particles.[45]

Conclusion

This work improves upon an earlier publication[21] that presented the $n(\nu)$ and $k(\nu)$ spectra for liquids in the MIR from

7800 to 400 cm^{-1} by introducing optimized methodologies to derive the $n(\nu)$ and $k(\nu)$ spectra over an expanded spectral range from 10 000 to 400 cm^{-1} at a spectral resolution of 2 cm^{-1}. The diverse set of the 111 liquids that were measured with these new protocols is provided in Supplemental Material (Table S1). The use of multiple path lengths (2 to 4000 μm) proved essential for improving the dynamic range and measurement accuracy, particularly with short cells for obtaining linear behavior from strong absorption features in the MIR, and with long cells for improving the SNR in the NIR. This improved SNR in the NIR enables measurements of weak absorption features, improving the accuracy of $n(\nu)$ and $k(\nu)$ values above 3500 cm^{-1}, specifically with a SNR improvement of more than tenfold for data above approximately 6500 cm^{-1}. For typical liquids, ~3% uncertainty in the amplitude of the k vector is calculated whereas the n vector uncertainty is typically ~0.4%, arising mostly from the estimate of $n(\nu_{max})$. Judicious choice of cell materials and path lengths must be optimized to yield the most accurate results. Finally, the derived $n(\nu)$ and $k(\nu)$ data from different researchers were used to model the absorbance spectra for aerosol droplets of 2-methylcyclohexanol, demonstrating that typical measurement uncertainties for n/k have a minimal impact on the predicted spectra. This expanded dataset of $n(\nu)$ and $k(\nu)$ can be used to build better spectral libraries for in situ and standoff detection of many chemicals, by accounting for different morphological parameters that will be present in real-world environments and enabling detection in both the MIR and NIR spectral regimes to improve detection confidence. These data support a wide range of applications including chemical detection, atmospheric science, remote sensing, and spectroscopy. Finally, improvements that reduce the dependence of the operator in the processing workflow such as automated data processing methods are being considered for future efforts.

Declaration of Conflicting Interests

The author(s) declared no potential conflicts of interest with respect to the research, authorship, and/or publication of this article.

Funding

The author(s) disclosed receipt of the following financial support for the research, authorship, and/or publication of this article: The research is based upon work supported in part by the Office of the Director of National Intelligence (ODNI), Intelligence Advanced Research Projects Activity (IARPA), via DOE DE-AC05-76RL01830. The views and conclusions contained herein are those of the authors and should not be interpreted as necessarily representing the official policies or endorsements, either expressed or implied, of the ODNI, IARPA, or the U.S. Government. The U.S. Government is authorized to reproduce and distribute reprints for Governmental purposes notwithstanding any copyright annotation thereon. PNNL is operated by Battelle for the U.S. Department of Energy (DOE) under Contract no. DE-AC05-76RL01830.

Data Availability

The final n/k data for the liquids listed in Table S1 are available to download from https://doi.org/10.25584/2997107.

ORCID iDs

Oliva M. Primera-Pedrozo https://orcid.org/0000-0002-6109-2020
Tracy J. Baker https://orcid.org/0000-0003-4508-3471
Schuyler P. Lockwood https://orcid.org/0000-0003-3582-5179
Ashley M. Bradley https://orcid.org/0000-0001-7344-9640
Timothy J. Johnson https://orcid.org/0000-0001-9514-6288
Tanya L. Myers https://orcid.org/0000-0001-8995-7033

Supplemental Material

All supplemental material mentioned in the text is available in the online version of the journal.

References

1. J. Uotila, J. Kauppinen. "Fourier Transform Infrared Measurement of Solid-, Liquid-, and Gas-Phase Samples with a Single Photoacoustic Cell". Appl. Spectrosc. 2008. 62(6): 655–660. 10.1366/000370208784658048
2. T.J. Baker, R.G. Tonkyn, C.J. Thompson, M.K. Dunlap, et al. "An Infrared Spectral Database for Gas-phase Quantitation of Volatile Per- and Polyfluoroalkyl Substances (PFAS)". J. Quant. Spectrosc. Radiat. Transfer. 2023. 295: 108420. 10.1016/j.jqsrt.2022.108420
3. M.D.W. Schneider, T.J. Baker, N.K. Scharko, T.A. Blake, et al. "A Method for Generating Quantitative Vapor-Phase Infrared Spectra of Solids: Results for Phenol, Camphor, Menthol, Syringol, Dicyclopentadiene, and Naphthalene". J. Quant. Spectrosc. Radiat. Transfer. 2024. 323: 109045. 10.1016/j.jqsrt.2024.109045
4. J.-M. Thériault, E. Puckrin, J. Hancock, P. Lecavalier, et al. "Passive Standoff Detection of Chemical Warfare Agents on Surfaces". Appl. Opt. 2004. 43(31): 5870–5885. 10.1364/AO.43.005870
5. R. Harig, R. Braun, C. Dyer, C. Howle, B. Truscott. "Short-Range Remote Detection of Liquid Surface Contamination by Active Imaging Fourier Transform Spectrometry". Opt. Express. 2008. 16(8): 5708–5714. 10.1364/OE.16.005708
6. J.-M. Thériault, E. Puckrin, H. Lavoie. "Remote Monitoring of Multi-Gas Mixtures by Passive Standoff Fourier Transform Infrared Radiometry". Appl. Spectrosc. 2007. 61(6): 630–637. 10.1366/000370207781269882
7. D. Schymanski, B.E. Oßmann, N. Benismail, K. Boukerma, et al. "Analysis of Microplastics in Drinking Water and Other Clean Water Samples with Micro-Raman and Micro-Infrared Spectroscopy: Minimum Requirements and Best Practice Guidelines". Anal. Bioanal. Chem. 2021. 413(24): 5969–5994. 10.1007/s00216-021-03498-y
8. W. Luo, P. Tian, G. Fan, W. Dong, et al. "Non-Destructive Determination of Four Tea Polyphenols in Fresh Tea Using Visible and Near-Infrared Spectroscopy". Infrared Phys. Technol. 2022. 123: 104037. 10.1016/j.infrared.2022.104037
9. M. Wang, X. Wang, Q. Xia, M. Liu, et al. "Application of Spectroscopy Technology in Detecting Toxic Effects of

Environmental Pollutants". Proc. SPIE. 2024. 13283: 132832P. 10.1117/12.303688
10. X. Li, X. Tang, H. Chen, T. Wu, B. Wang. "Quantitative Analysis Method for the Fourier Transform Infrared Spectroscopy of Gases". Proc. SPIE. 2024. 12972: 129720J. 10.1117/12.3022573
11. M. Moniz Vieira Pinto, V.G. Poli de Lima, L.J. Raniero, E.A. Lo Schiavo Arisawa. "Saliva Diagnosis of Autistic Spectrum Disorder by FT-IR Spectroscopy". Proc. SPIE. 2021. 11660: 116600E. 10.1117/12.2583257
12. K.A. Frings, L. Baumann, N. Heine, N. Debener, et al. "Spectroscopic Analysis and Classification of Oral Bacteria in Mixed Samples Using FT-IR Spectroscopy and Deep Learning". Proc. SPIE. 2025. 13331: 1333104. 10.1117/12.3042855
13. K.A. Peterson, R.M. Francis, C.A. Banach, A.M. Bradley, et al. "Method to Derive the Infrared Complex Refractive Indices *n* (λ) and *k*(λ) for Organic Solids from KBr Pellet Absorption Measurements". Appl. Opt. 2024. 63(6): 1553–1565. 10.1364/AO.514661
14. C.A. Banach, A.M. Bradley, R.G. Tonkyn, O.N. Williams, et al. "Dynamic Infrared Gas Analysis from Longleaf Pine Fuel Beds Burned in a Wind Tunnel: Observation of Phenol in Pyrolysis and Combustion Phases". Atmos. Meas. Tech. 2021. 14(3): 2359–2376. 10.5194/amt-14-2359-2021
15. K.D. Hughey, R.G. Tonkyn, W.W. Harper, V.L. Young, et al. "Preliminary Studies of UV Photolysis of Gas-Phase CH_3I in Air: Time-Resolved Infrared Identification of Methanol and Formaldehyde Products". Chem. Phys. Lett. 2021. 768: 138403. 10.1016/j.cplett.2021.138403
16. C.J. Thompson, N.B. Gallagher, K.D. Hughey, M.K. Dunlap, et al. "An Interactive Spectral Analysis Tool for Chemical Identification and Quantification of Gas-Phase Species in Complex Spectra". Appl. Spectrosc. 2023. 77(6): 557–568. 10.1177/00037028231169304
17. F. Radica, G. Della Ventura, L. Malfatti, M. Cestelli Guidi, et al. "Real-time Quantitative Detection of Styrene in Atmosphere in Presence of Other Volatile-Organic Compounds Using a Portable Device". Talanta. 2021. 233: 122510. 10.1016/j.talanta.2021.122510
18. J.F. Mustard, J.E. Hays. "Effects of Hyperfine Particles on Reflectance Spectra from 0.3 to 25 μm". Icarus. 1997. 125(1): 145–163. 10.1006/icar.1996.5583
19. M.D. Lane. "Midinfrared Optical Constants of Calcite and Their Relationship to Particle Size Effects in Thermal Emission Spectra of Granular Calcite". J. Geophys. Res.: Planets. 1999. 104(E6): 14099–14108. 10.1029/1999JE900025
20. J.E. Moersch, P.R. Christensen. "Thermal Emission from Particulate Surfaces: A Comparison of Scattering Models with Measured Spectra". J. Geophys. Res.: Planets. 1995. 100(E4): 7465–7477. 10.1029/94JE03330
21. T.L. Myers, R.G. Tonkyn, T.O. Danby, M.S. Taubman, et al. "Accurate Measurement of the Optical Constants *n* and *k* for a Series of 57 Inorganic and Organic Liquids for Optical Modeling and Detection". Appl. Spectrosc. 2018. 72(4): 535–550. 10.1177/0003702817742848
22. R. Tonkyn, T. Danby, J. Birnbaum, M. Taubman, et al. "Measurement of Infrared Refractive Indices of Organic and Organophosphorous Compounds for Optical Modeling". Proc. SPIE. 2017. 10183: 1018306. 10.1117/12.2264384
23. T.L. Myers, R.G. Tonkyn, T.O. Danby, B.M. De Vetter, et al. "Accurate Measurement of the Optical Constants for Modeling Organic and Organophosphorous Liquid Layers and Drops". Proc. SPIE. 2018. 10629: 1062912. 10.1177/0003702817742848
24. B.E. Bernacki, T.J. Johnson, T.L. Myers. "Modeling Thin Layers of Analytes on Substrates for Spectral Analysis: Use of Solid/Liquid *n* and *k* Values to Model Reflectance Spectra". Opt. Eng. 2020. 59(9): 092005. 10.1117/1.oe.59.9.092005
25. B.E. Bernacki, T.J. Johnson, T.L. Myers, T.A. Blake. "Modeling Liquid Organic Thin Films on Substrates". Proc. SPIE. 2018. 10629: 1062916. 10.1117/12.2299873
26. N.J. Harrick, K.H. Beckmann. "Internal Reflection Spectroscopy". In: P.F. Kane, G.B. Larrabee, editors. Characterization of Solid Surfaces. New York: Plenum Press, 1974. Pp. 215–245. 10.1007/978-1-4613-4490-2_11
27. P.R. Griffiths, J.A. De Haseth, J.D. Winefordner. "Quantitative Analysis". In: P.R. Griffiths, J.A. de Haseth, et al. Fourier Transform Infrared Spectrometry. Hoboken, New Jersey: Wiley-Interscience, 2007. Ch. 9, Pp. 197-224. 10.1002/9780470106310.ch9
28. B.C. Smith. Infrared Spectral Interpretation: A Systematic Approach. Boca Raton, Florida: CRC Press, 1998.
29. C.M. Tonauer, E.-M. Köck, R. Henn, J.N. Stern, et al. "Near-Infrared Spectroscopy for Remote Sensing of Porosity, Density, and Cubicity of Crystalline and Amorphous H_2O Ices in Astrophysical Environments". Astrophys. J. 2024. 970(1): 82. 10.3847/1538-4357/ad4f82
30. P. Wu, H.W. Siesler. "The Assignment of Overtone and Combination Bands in the near Infrared Spectrum of Polyamide 11". J. Near Infrared Spectrosc. 1999. 7(2): 65–76. 10.1255/jnirs.236
31. R. Claps, F.V. Englich, D.P. Leleux, D. Richter, et al. "Ammonia Detection by Use of Near-Infrared Diode-Laser-Based Overtone Spectroscopy". Appl. Opt. 2001. 40(24): 4387–4394. 10.1364/AO.40.004387
32. R.A. Viscarra Rossel, R.N. McGlynn, A.B. McBratney. "Determining the Composition of Mineral-Organic Mixes Using UV–Vis-NIR Diffuse Reflectance Spectroscopy". Geoderma. 2006. 137(1): 70–82. 10.1016/j.geoderma.2006.07.004
33. R. Iwamoto, A. Nara, T. Matsuda. "Near-Infrared Combination and Overtone Bands of the CH_2 Sequence in CH_2X_2, CH_2XCHX_2, and $CH_3(CH_2)_5CH_3$ and their Characteristic Frequency Zones". Appl. Spectrosc. 2006. 60(4): 450–458. 10.1366/00037020577747831 79
34. M. Ventura, J.R. Silva, T. Catunda, L.H.C. Andrade, S.M. Lima. "Identification of Overtone and Combination Bands of Organic Solvents by Thermal Lens Spectroscopy with Tunable Ti:Sapphire Laser Excitation". J. Mol. Liq. 2021. 328: 115414. 10.1016/j.molliq.2021.115414
35. R. Iwamoto, A. Nara, T. Matsuda. "Near-Infrared Combination and Overtone Bands of CH in CHX_3, CHX_2–CHX_2, and CHX_2–CX_2–CHX_2". Appl. Spectrosc. 2005. 59(11): 1393–1398. 10.1366/000370205774783179
36. T.L. Myers, R.G. Tonkyn, A.M. Oeck, T.O. Danby, et al. "IARPA/PNNL Liquid Phase IR Spectra". https://webbook.nist.gov/chemistry/silmarils-liquids-n-k/ [accessed 6 November 2025].
37. T.L. Myers, R.G. Tonkyn, J.S. Loring, A.M. Oeck, et al. "Accurate Optical Constants for Liquids in the Near-Infrared: Improved Methods for Obtaining *n* and *k* from 1 to 4 μm". Proc. SPIE. 2019. 11010: 110100O. 10.1117/12.2519499

38. J.E. Bertie, C.D. Keefe. "Infrared Intensities of Liquids XXIV: Optical Constants of Liquid Benzene-h_6 at 25°C Extended to 11.5 cm^{-1} and Molar Polarizabilities and Integrated Intensities of Benzene-h_6 Between 6200 and 11.5 cm^{-1}". J. Mol. Struct. 2004. 695: 39–57. 10.1016/j.molstruc.2003.11.002
39. J.E. Bertie, C.D. Keefe, R.N. Jones. "Infrared Intensities of Liquids VIII. Accurate Baseline Correction of Transmission Spectra of Liquids for Computation of Absolute Intensities, and the 1036 cm^{-1} Band of Benzene as a Potential Intensity Standard". Can. J. Chem. 1991. 69(11): 1609–1618. 10.1139/v91-236
40. J.E. Bertie, K.H. Michaelian. "Comparison of Infrared and Raman Wave Numbers of Neat Molecular Liquids: Which is the Correct Infrared Wave Number to Use?". J. Chem. Phys. 1998. 109(16): 6764–6771. 10.1063/1.477322
41. J.E. Bertie, S.L. Zhang, C. Dale Keefe. "Measurement and Use of Absolute Infrared Absorption Intensities of Neat Liquids". Vib. Spectrosc. 1995. 8(2): 215–229. 10.1016/0924-2031(94)00038-I
42. J.E. Bertie, S.L. Zhang, C.D. Keefe. "Infrared Intensities of Liquids XVI. Accurate Determination of Molecular Band Intensities from Infrared Refractive Index and Dielectric Constant Spectra". J. Mol. Struct. 1994. 324(1): 157–176. 10.1016/0022-2860(94)08237-5
43. J.E. Bertie. "John Bertie's Download Site". https://sites.ualberta.ca/~jbertie/JBDownload.HTM [accessed 6 November 2025].
44. T.L. Myers, B.E. Bernacki, M.J. Wilhelm, K.L. Jensen, et al. "Influence of Intermolecular Interactions on the Infrared Complex Indices of Refraction for Binary Liquid Mixtures". Phys. Chem. Chem. Phys. 2022. 24(36): 22206–22221. 10.1039/d2cp02920k
45. S.P. Lockwood, B.E. Bernacki, M.J. Wilhelm, T.L. Myers, et al. "Modeling Aerosol Transmission Spectra from $n(\lambda)$ and $k(\lambda)$ Infrared Optical Constants Measurements of Organic Liquids and Solids". Opt. Express. 2024. 32(17): 30169–30181. 10.1364/OE.529439
46. S.W. Sharpe, T.J. Johnson, R.L. Sams, P.M. Chu, et al. "Gas-Phase Databases for Quantitative Infrared Spectroscopy". Appl. Spectrosc. 2004. 58(12): 1452–1461. 10.1366/0003702042641281
47. T.J. Johnson, T.J. Baker, A.M. Bradley, M.O. Yokosuk, T.L. Myers. "Twice-Modulated Light in Fourier Transform Infrared (FT-IR) Spectrometers from Reflective Samples: Avoiding Distorted Intensity Values". Appl. Spectrosc. 2022. 76(5): 620–624. 10.1364/AS.76.000620
48. W.R.M. Rocha, S. Pilling. "Determination of Optical Constants *n* and *k* of Thin Films from Absorbance Data Using Kramers–Kronig Relationship". Spectrochim. Acta, Part A. 2014. 123: 436–446. 10.1016/j.saa.2013.12.075
49. B. Tatian. "Fitting Refractive-index Data with the Sellmeier Dispersion Formula". Appl. Opt. 1984. 23(24): 4477–4485. 10.1364/AO.23.004477
50. J. Schäfer, S.C. Lee, A. Kienle. "Calculation of the Near Fields for the Scattering of Electromagnetic Waves by Multiple Infinite Cylinders at Perpendicular Incidence". J. Quant. Spectrosc. Radiat. Transfer. 2012. 113(16): 2113–2123. 10.1016/j.jqsrt.2012.05.019
51. J. Schäfer. "MatScat v.1.4.0.0 ". http://www.mathworks.com/matlabcentral/fileexchange/36831-matscat [accessed 6 November 2025].
52. J.M.O. Salcido, S. Lockwood, A. Zelenyuk, T. Baker, et al. "Quantitative Infrared Spectroscopy of Aerosols: Mie Theory Modeling with Experimental Validation". Optica. 2025. 12(9): 1462–1468. 10.1364/OPTICA.566710
53. M.I. Cotterell, J.W. Knight, J.P. Reid, A.J. Orr-Ewing. "Accurate Measurement of the Optical Properties of Single Aerosol Particles Using Cavity Ring-Down Spectroscopy". J. Phys. Chem. A. 2022. 126(17): 2619–2631. 10.1021/acs.jpapproximately2c01246
54. J.E. Bertie, H.H. Eysel. "Infrared Intensities of Liquids I: Determination of Infrared Optical and Dielectric Constants by FT-IR Using the CIRCLE ATR Cell". Appl. Spectrosc. 1985. 39(3): 392–401. 10.1366/0003702854248575
55. T.J. Johnson, S.W. Sharpe, M.A. Covert. "Disseminator for Rapid, Selectable, and Quantitative Delivery of Low and Semivolatile Liquid Species to the Vapor Phase". Rev. Sci. Instrum. 2006. 77(9). 10.1063/1.2349298